ELSEVIER

Polymer 42 (2001) 9551–9564

polymer

www.elsevier.com/locate/polymer

Micromechanisms of slow crack growth in polyethylene under constant tensile loading

Christopher J.G. Plummer[a,*], Anne Goldberg[b], Antoine Ghanem[c]

[a]*Laboratoire de Polymères (LP), Ecole Polytechnique Fédérale de Lausanne (EPFL), CH-1015 Lausanne, Switzerland*
[b]*Solvay Polyolefins Europe, 310 Rue de Ransbeek, 1120 Brussels, Belgium*
[c]*Solvay Research and Technology Centre, 310 Rue de Ransbeek, 1120 Brussels, Belgium*

Received 26 March 2001; received in revised form 22 June 2001; accepted 29 June 2001

Abstract

Circumferentially notched specimens of a first generation and a third generation pipe-grade of high density polyethylene with similar weight average molar masses have been subjected to constant tensile loads at 80°C. A transition from full ligament yielding to failure by stable sub-critical crack growth was observed as the applied load was decreased. The specimen lifetimes in this latter regime were dependent on the initial stress intensity factor, K_i, and failure was associated with slow crack propagation preceded by formation of a wedge-shaped cavitational deformation zone at the notch tip. The fibril diameters in the deformation zones decreased with stress intensity factor near the transition, the limiting behaviour of a relatively slow crack growth resistant third generation grade at the lowest K_i being inferred from testing in Igepal™ to be the breakdown of diffuse zones of interlamellar voiding. This regime was not directly accessible to testing in air within the allotted experimental times. However, comparison with the results of accelerated testing in cyclic fatigue has indicated stable interlamellar voiding in the third generation grade not to necessitate the presence of Igepal. Moreover, in both grades, very similar modes of deformation were observed in air and in Igepal at relatively high K_i. Igepal was therefore inferred not to lead to qualitative changes in the range of mechanisms that are characteristic of slow crack growth in polyethylene.

Keywords: Polyethylene; Microdeformation; Slow crack growth

1. Introduction

Current interest in slow crack growth (SCG) in polyethylene (PE) is motivated by practical concerns over its long term performance in service, where it may be subject to significant pressures and contact with water or other industrial fluids. Hydrostatic pressure testing of pipes is still widely used to assess their performance. However, for many modern PE grades, failure times may be of the order of years [1]. Pre-screening of different grades therefore generally involves accelerated testing, usually of notched specimens either taken from a pipe or moulded ad hoc. Accelerated SCG can be achieved by testing at high temperature and/or in the presence of a surfactant and/or under cyclic loading conditions. Non-ionic surfactants such as Igepal™ (nonyl phenol ether glycol) [2] are particularly effective for reducing the failure times of the tougher materials without affecting their ranking with respect to other grades tested under the same conditions. Indeed, according to Fleissner, "surfactant-assisted stress cracking is a means to markedly reduce testing time *without changing the failure mechanism*" [3]. This is important if such tests are to be of direct relevance to a wide range of service conditions, although the fundamental reasons for such behaviour remain unclear [4].

In the present study, we have used various microscopical techniques to examine the microdeformation mechanisms associated with SCG under tensile loading in two grades of high density PE (HDPE) at 80°C in air and in Igepal. The aim was to gain insight into the micromechanisms of long-term failure in these materials and the differences in the behaviour of the different grades. The work was also motivated by our interest in the extent to which Igepal results in qualitative modifications in microdeformation behaviour, and hence the extent to which accelerated testing is representative of failure in air under conditions not accessible to experiment within convenient times.

2. Experimental

2.1. Materials

The HDPE grades used in this study were two pipe-grade

* Corresponding author. Tel.: +41-21-693-2856; fax: +41-21-693-5868.
E-mail address: christopher.plummer@epfl.ch (C.J.G. Plummer).

0032-3861/01/$ - see front matter
PII: S0032-3861(01)00476-1

Table 1
Materials data for polymers PEA and PEB

Resin	Density (kg/m^3)	M_n (kdA)	M_w (kdA)
PEA: 1st generation	956	9.1	236
PEB: 3rd generation	959	9.1	215

ethylene–butene copolymers (PEA and PEB) from Solvay, with similar melt flow indices and densities. Data for the two materials are given in Table 1.

2.2. Mechanical testing

All the mechanical tests to be described in what follows were performed on notched specimens, under creep loading conditions and at a temperature of 80°C. As discussed in the introduction, the resistance to SCG may be investigated using a range of techniques. However, since part of our aim was to compare results from the test methods that are currently most widespread in the literature, we opted for the test geometries and conditions listed below.

2.3. Cylindrical notched bar (CNB) tests in air

For creep testing in air, use was made of cylindrical circumferentially notched specimens (Fig. 1(a)) machined from compression moulded plaques. The presence of a notch around the entire perimeter of a tensile test specimen promotes plane strain in the remaining ligament so that necking tends to be suppressed in favour of SCG under creep conditions. It follows that SCG tests can be performed at relatively high loads using such specimens, allowing one to reduce the overall test times.

The specimen diameter was 12 mm, the total specimen length was 60 mm and the machined notch depth was generally about 2 mm. A pre-crack was introduced to the notch

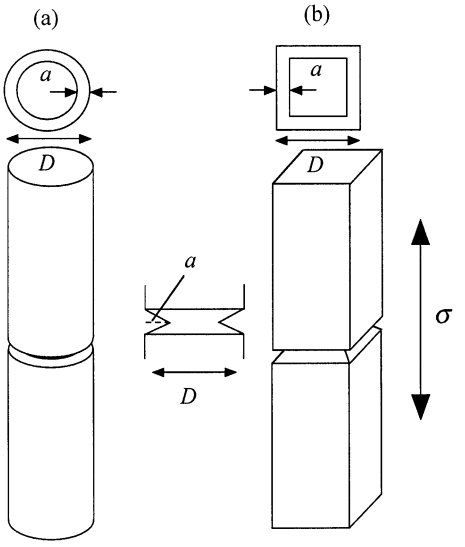

Fig. 1. (a) Cylindrical notched bar (CNB) specimen geometry and (b) full notch creep test (FNCT) specimen geometry.

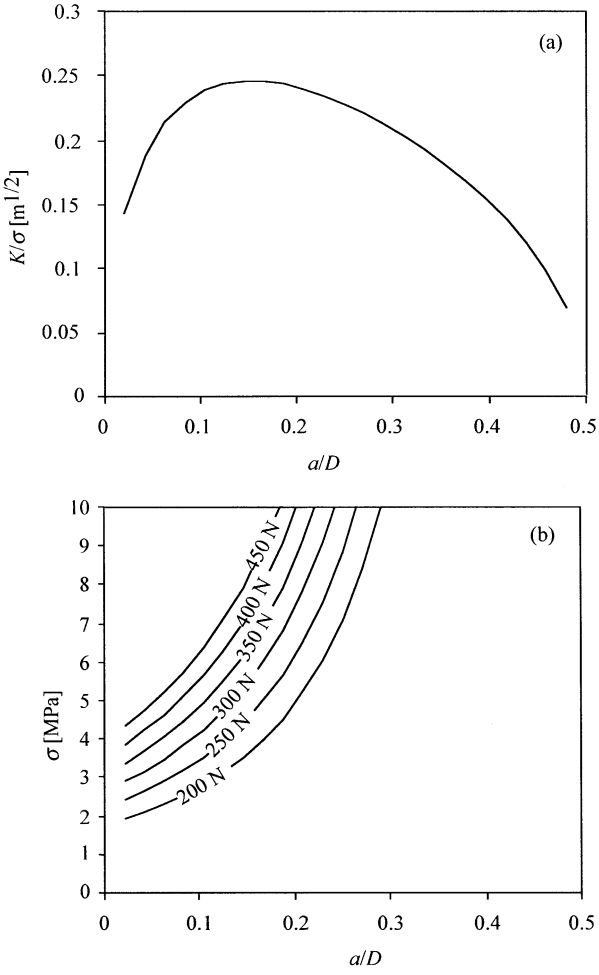

Fig. 2. (a) K/σ as a function of a/D for $D = 12$ mm; (b) σ as a function of a/D for various values of F.

tip using a fresh razor blade. The tests were carried out at 80°C in force control mode using a Zwick 1400 screw driven machine equipped with an air oven. After clamping the specimen at zero load and tempering for 1 h at 80°C, various fixed loads were applied and the displacement of the lower (mobile) specimen end recorded using a mechanical extensometer. The crack length used to calculate the initial values of the stress intensity, K_i, and the ligament stress, σ, was determined by inspection of the fracture surface after completion of each test. The maximum test time was limited to about two months.

The stress intensity factor in a CNB specimen with a sharp notch subject to a tensile load F is given in Ref. [5]

$$K = \sigma_{nom}(\pi a(1-2\xi))^{1/2} \times \left(\frac{1.121 - 3.08\xi + 7.344\xi^2 - 10.244\xi^2 + 5.85\xi^4}{1 - 4\xi + 4\xi^2}\right) \quad (1)$$

where ξ is the reduced crack length a/D, D is the total

Table 2
Summary of the test and materials parameters

Resin	Sample n°	Colour	Geometry	Environment	Processing
PEA	PE1	Black	CNB	Air	Compression moulding
PEB	PE2	Black	CNB	Air	Compression moulding
PEA	PE3	Natural	FNCT	Igepal	Compression moulding
PEB	PE4	Black	FNCT	Igepal	Compression moulding
PEB	PE5	Black	FNCT	Igepal	Pipe

specimen diameter, $\sigma_{nom} = 4F/\pi D^2$, and

$$\sigma = 4F/\pi(D - 2a)^2 \quad (2)$$

K/σ showed a maximum at a/D of about 0.18 (Fig. 2(a)) which was the reason for choosing 2 mm to be the default notch depth, that is, the approximate initial crack length. If plane strain conditions are assumed, the critical ligament stress for plastic collapse should be independent of a (for simplicity, we ignore the time dependence of the yield stress, σ_y). Given that σ increases rapidly with a/D (Fig. 2(b)), crack propagation in this geometry is therefore expected to lead to ductile necking of the central part of the ligament, unless the fibrillar crack tip deformation zone characteristic of SCG in PE is able to propagate across its entire width first [6,7].

2.4. Full notch creep tests (FNCT) in Igepal

The tests in Igepal were carried out using the FNCT geometry (Fig. 1(b)), which is now widely used in the pipe community [8–11]. In this case, the specimens take the form of a rectangular parallelepiped with dimensions $10 \times 10 \times 100\ mm^3$. A notch of uniform depth was introduced by gently pushing a razor blade into the specimen at its mid-point, so that the remaining ligament was square in cross-section. The specimens were loaded using commercial creep loading apparatus (IPT, Germany) at 80°C in 2% Igepal CO-630 in demineralised water, after tempering for 1 h at the test temperature. The initial loading rate was 72 MPa/min.

K_i was calculated numerically using the ABAQUS® finite element package, there being no analytical expressions available for this geometry to our knowledge. The calculations indicated the stress intensity to be heterogeneous, increasing with distance from the centre of the ligament sides, to reach a maximum at the corners. Thus, for an initial ligament stress, σ_i of 3 MPa, we obtained $K_i^{min} = 0.12\ MPam^{1/2}$ and $K_i^{max} = 0.3\ MPam^{1/2}$. However, K_i^{min} was observed to control the SCG rate under these conditions and for a given σ_i, $K_i^{min} = K_i$, where K_i is the value calculated for CNB specimens using Eq. (1) [12]. This result has been confirmed elsewhere in the literature [8]. K_i was therefore taken to be the effective initial stress intensity factor in both geometries.

2.5. Summary of the test and materials parameters

The full range of materials and test parameters used in the present investigation are summarised in Tables 1 and 2. Most of the specimens were pigmented using carbon black and with the exception of PE5, which was machined from an extruded pipe, they were all prepared by compression moulding.

2.6. Microscopy

After the tests, the fracture surfaces were trimmed and embedded in either an epoxy resin (Araldite D from Ciba) or distilled methyl methacrylate (MMA) containing a few wt% benzoyl peroxide. The epoxy was cured at room temperature, whereas the MMA was polymerised overnight at 40°C and post-cured at 80°C for a further 24 h. In general, embedding in epoxy gave better contrast owing to preferential staining of the specimen-epoxy interfaces, but MMA gave better penetration. Positive or negative staining of the HDPE was observed for both types of embedding medium, depending on the depth at which the sections were taken and the degree of penetration of internal voids by the resin and/or the stain.

An ultramicrotome (Reichert–Jung Ultracut E) and a 2.5 mm wide 35 or 45° diamond knife (Diatome) were used for sectioning. A trapezoidal surface not exceeding 1.5 mm in width was prepared using a trimming knife and semi-thin sections (about 10 μm) removed for optical microscopy (OM) using a glass knife. The specimen was then exposed to RuO_4 vapour overnight by placing it over a watch glass containing 50 mg of $RuCl_3 \cdot 3H_2O$ mixed with 2.5 ml of 5% aqueous NaClO. After staining, sections of between 50 and 100 nm in thickness were prepared at room temperature and picked up from distilled water onto copper TEM grids covered with a thin film of carbon.

Transmission electron microscopy (TEM) was carried out using a Philips EM430 (accelerating voltage 300 kV), or a Philips CM 20 (200 kV), depending on the availability of the microscopes. The fracture surfaces were also observed by scanning electron microscopy (SEM) (Philips XL-30, equipped with a field emission gun) at about 2 kV. The carbon filled specimens generally showed little charging and could easily be observed at up to 5 kV, but beam damage in the form of coalescence of fine structure was more marked under these conditions.

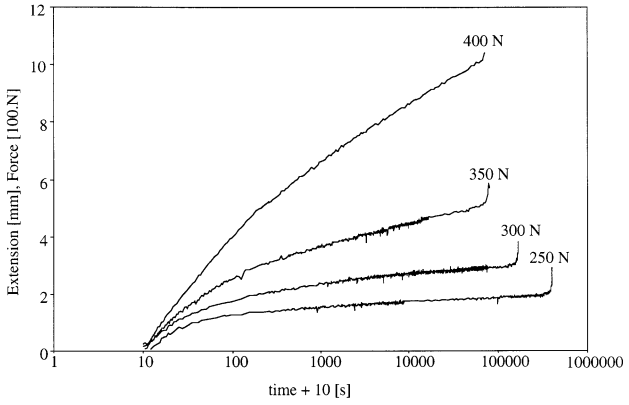

Fig. 3. Creep curves for PEA tested under different loads.

3. Results

3.1. CNB testing in air (series PE1 and PE2)

Fig. 3 shows creep curves from PEA specimens loaded at different ligament stresses, illustrating the three distinct regimes typical of this type of test. The initially large deformation rate corresponded to the application of the load, the period of transient loading lasting about 30 s in this case. The subsequent evolution of the global strain was dominated by the deformation of the ligament defined by the notch, associated with stable necking and/or SCG at the notch tip, depending on the applied load. The onset of the final stage of the deformation process corresponded to either unstable necking or crack advance through the damage zone at the crack tip. Since this was characterised by a rapid acceleration of the deformation rate, the overall failure times in the SCG regime were strongly correlated with the initiation times for crack advance. They were therefore expected to depend primarily on K_i.

For notched specimens of both PEA and PEB, $\sigma_y \approx 9$ MPa at 80°C at a constant loading rate of 10 mm/min, and fully ductile behaviour occurred after short times at comparable values of the initial ligament stress, σ_i. The lengths of the crack tip deformation zones observed at lower σ_i did not exceed 2 mm, becoming very much less than 2 mm at the lowest stresses investigated. Hence, residual necking in the central part of the fracture surface tended to persist over the whole range of test conditions studied, regardless of whether failure initiated by SCG.

Fig. 4(a) shows σ_i plotted against time to failure for PEA specimens and for two different notch depths, and Fig. 4(b) shows K_i against time to failure for the same specimens. These results confirm the specimen lifetime to be K_i controlled over most of the range of loads investigated. The high K_i plateau in Fig. 4(b) was characterised by extensive plastic necking prior to failure and the failure time was assumed to be dominated by the kinetics of the yielding process. Beyond this plateau, a sharp drop in K_i with increasing failure time marked the transition to SCG [12–15].

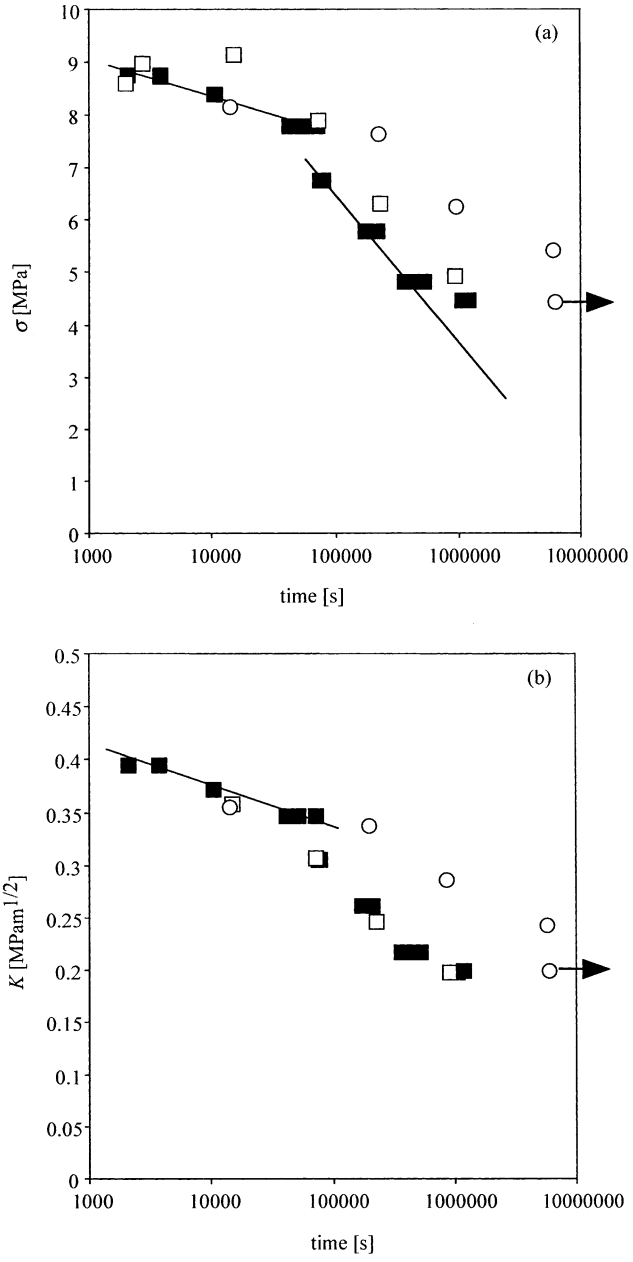

Fig. 4. (a) σ plotted against failure time for PEA and PEB and (b) K plotted against failure time for the same specimens. The open and filled squares are for PEA and for notch depths of approximately 2 and 4 mm, respectively. The circles are for PEB and a notch depth of approximately 2 mm.

The results for PEB specimens are also shown in Fig. 4. The high load regime of ductile behaviour was similar to that observed for PEA. However the transition to SCG behaviour was significantly delayed, and neither failure nor SCG could be observed in PEB at the lowest K_i within the allotted test times.

3.2. CNB fracture surfaces in air (series PE1 and PE2)

For the reasons outlined in the previous section, a neck was observed at the centre of all the fracture surfaces, its

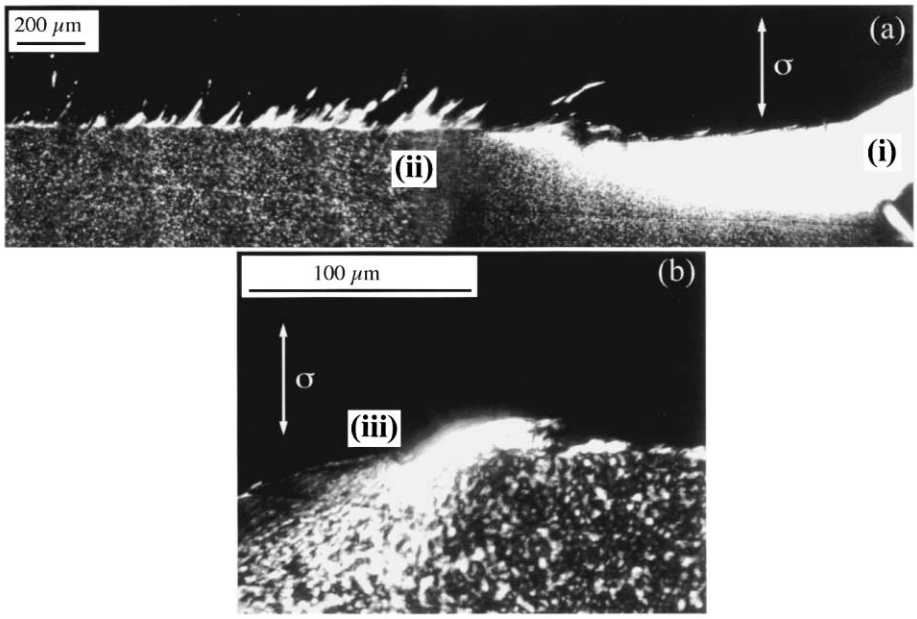

Fig. 5. OM of the fracture surface of a PEA specimen tested to failure at $\sigma_i = 5$ MPa and $K_i = 0.22$ MPam$^{1/2}$ in air: (a) image taken between crossed polarisers of part of the central necked region of the fracture surface (i) and part of the surrounding fibrillar region (ii); (b) detail from the region containing the notch tip (iii) (tensile axis as indicated by the arrows).

size diminishing as K_i decreased (for a fixed notch depth). The fibril diameters in the regions of the fracture surfaces corresponding to SCG were also found to diminish with decreasing K_i. This was reflected by a decrease in the fibril diameter at the original notch tip as the load was decreased. Moreover, there was an increase in the fibril diameter toward the specimen centre for a given load, that is, in regions that were deformed after a certain amount of stable crack advance and hence for which K was assumed to be greater than K_i. This is shown in Figs. 5–7.

Fig. 5 shows images from polarised light microscopy (OM) of a section through the fracture surface of a PEA specimen tested to failure a $\sigma_i = 5$ MPa and $K_i = 0.22$ MPam$^{1/2}$, showing part of the central neck and the surrounding fibrillar region. This fibrillar region extended to the periphery of the fracture surface, although the presence of a relatively highly deformed region at the notch tip suggested some crack tip blunting in the early stages of SCG.

Fig. 6(a) is a TEM image from a thin section taken from just in front of the notch tip in the specimen shown in Fig. 5, where the fibrils were relatively fine. There was a sharp interface between the damage zone and the surrounding undeformed material. Moreover, the internal structure of this part of the deformation zone was relatively uniform through its thickness, indicating most of the deformation to have occurred at the interface. The fibrillar texture here was on about the same scale as the dominant lamellae [16], and indeed there was some continuity between the fibrils and lamellae adjacent to the interface, as is apparent from Fig. 6(a). Fig. 6(b) is from about 2 mm from the notch tip, showing a somewhat greater fibril spacing than in Fig. 6(a).

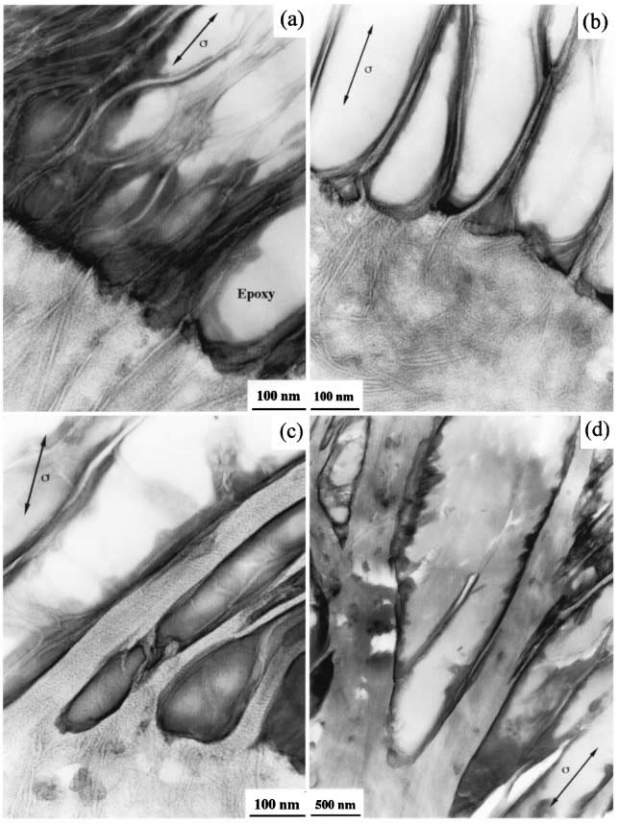

Fig. 6. TEM of a section through the fracture surface shown in Fig. 5: (a) section from just in front of the notch tip; (b) section from about 2 mm from the notch tip; (c) section from just outside the central neck; (d) section from behind the neck (tensile axis as indicated by the arrows).

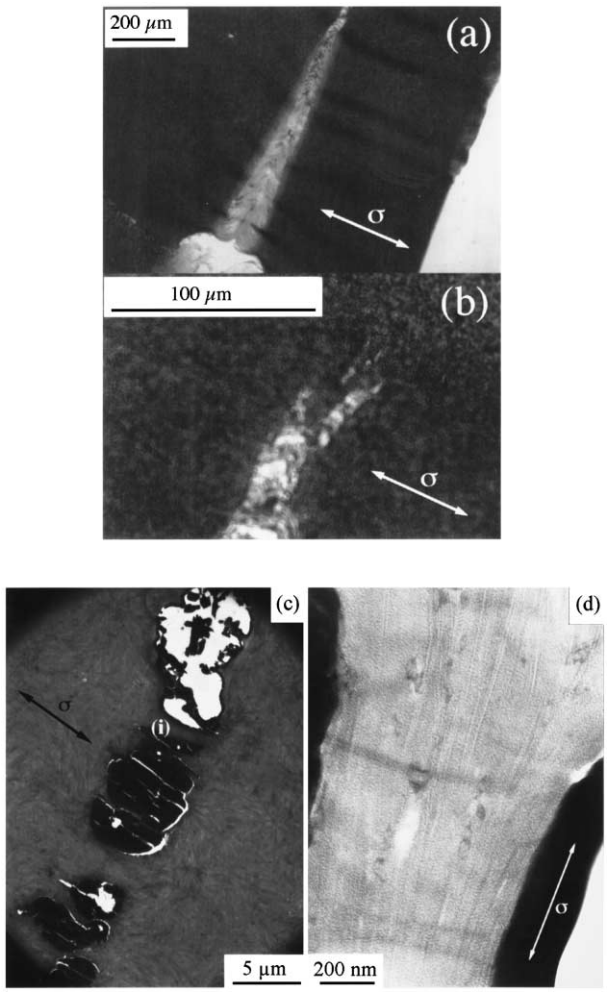

Fig. 7. The crack tip deformation zone in a PEA specimen tested at $\sigma_i = 7$ MPa and $K_i = 0.3$ MPam$^{1/2}$ in air: (a) overview of the deformation zone; (b) OM of the deformation zone tip; (c) low magnification TEM image of the deformation zone tip; (d) detail of the internal structure of the region marked (i) in (c) (tensile axis as indicated by the arrows).

Texture was also visible within the fibrils, certain of which appeared to consist of a bundle of 'sub-fibrils' associated with individual lamellae, drawn together in a finely voided, branched structure at the fibril base. However, the bulk of the deformation at the origin of the fibrillar texture in the interior of the deformation zone again appeared to have taken place at or close to the interface with the undeformed material.

Closer to the central neck the main fibrils were considerably coarser, although finer 'cross-tie' fibrils were still visible between them, as shown in Fig. 6(c). The existence of these cross-tie fibrils is significant in that they permit stress transfer perpendicular to the main fibril direction and hence promote stress concentration at the craze tip [17]. However, in the present case, the essentially two-dimensional images provided by the thin sections were potentially misleading, since high magnification SEM of the fracture surfaces indicated the matrix ligaments to be sheet-like. Thus the structure of the deformation zone was closer to that of a closed cell foam than to a truly fibrillar structure. This trend was even more marked at the specimen centre, the internal structure of the macroscopic neck being characterised by large isolated voids, which became extended along the deformation direction. Fig. 6(d) shows the early stages of voiding in the outer part of the neck, where the void density was relatively high. In addition to the intact cross-tie fibrils visible in Fig. 6(d), fibrillar debris was present at the void surfaces, indicating breakdown of crazes or craze-like structures during void formation. The internal structure of the deformed ligaments in Fig. 6(c) and (d) reflected a gradual drawing down of the bulk lamellar texture throughout the thickness of the deformation zone. The interface between the deformed and the undeformed material was consequently relatively poorly defined. In the more highly deformed regions of the macroscopic neck, continued drawing of the voided regions resulted in a pronounced layered texture. The central part of the neck, however, showed relatively limited voiding.

At $\sigma_i = 7$ MPa and $K_i = 0.3$ MPam$^{1/2}$, deformation in PEA was globally more ductile and the final stages of deformation involved more extensive necking than in the specimen described previously. The initial stages of failure were nevertheless still characterised by the formation of a crack tip deformation zone. Fig. 7 shows the structure of the tip of this deformation zone at various magnifications in a specimen which had been unloaded after a limited amount of SCG and the crack faces wedged open during embedding. The deformation zone extended a few 100 μm into the specimen, and consisted entirely of unconnected voids with necking of the intervening ligaments, which incorporated many individual lamellae. Relatively large, isolated voids were present at the deformation zone tip, visible optically in Fig. 7(b) and again as the heavily stained regions in Fig. 7(c) and (d) shows a detail of a partly deformed ligament between two such voids, in which the evolution of the lamellar texture suggests a relatively weak deformation gradient (cf. Fig. 6(c) and (d)). Owing to the highly interconnected nature of the matrix ligaments in this case, crack advance through the deformation zone tended to draw the material behind the crack tip towards the specimen centre. Hence, in spite of the highly inhomogeneous voided structure of the damage zone ahead of the crack tip, the peripheral regions of the fracture surfaces corresponding to SCG in specimens such as that in Fig. 7 appeared relatively smooth when observed by SEM or OM, and contiguous with the central neck.

For PEB tested in air, very similar behaviour was observed in the SCG regime to that in PEA for comparable K_i, although the failure times were much longer. Representative TEM micrographs from a specimen tested with $\sigma_i = 6$ MPa and $K_i = 0.26$ MPam$^{1/2}$ are given in Fig. 8, showing fibrillar structure from the periphery of the fracture surface (Fig. 8(a) and (b)) and coarser voiding from closer to the specimen centre (Fig. 8(c)). There is some suggestion of an

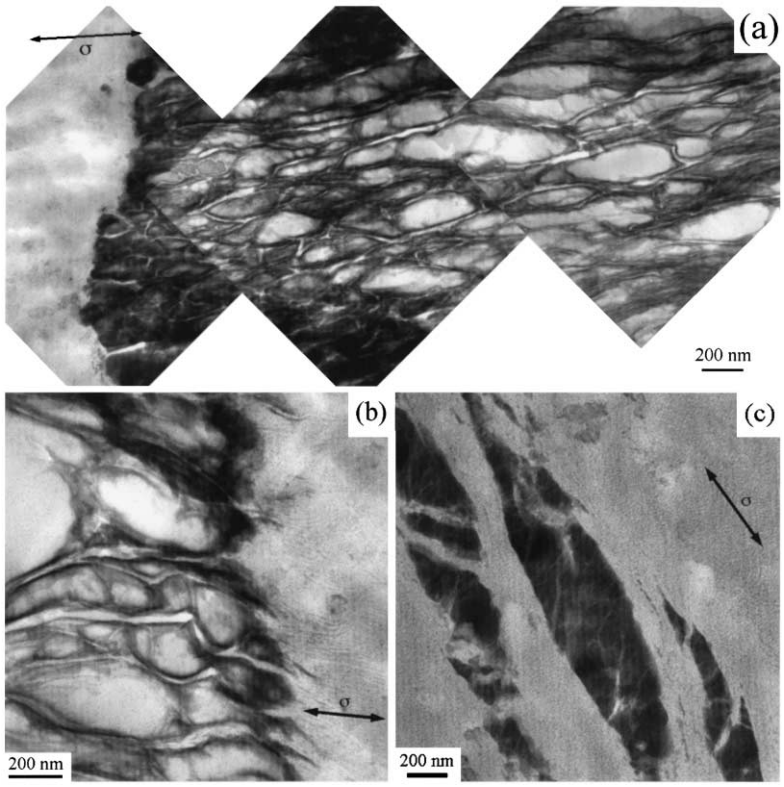

Fig. 8. The crack tip deformation zone in a PEB specimen tested at $\sigma_i = 6$ MPa and $K_i = 0.26$ MPam$^{1/2}$ in air: (a) fibrillar deformation at the periphery of the fracture surface; (b) detail of the edge of the deformation zone in (a); (c) voiding behind the central neck (tensile axis as indicated by the arrows).

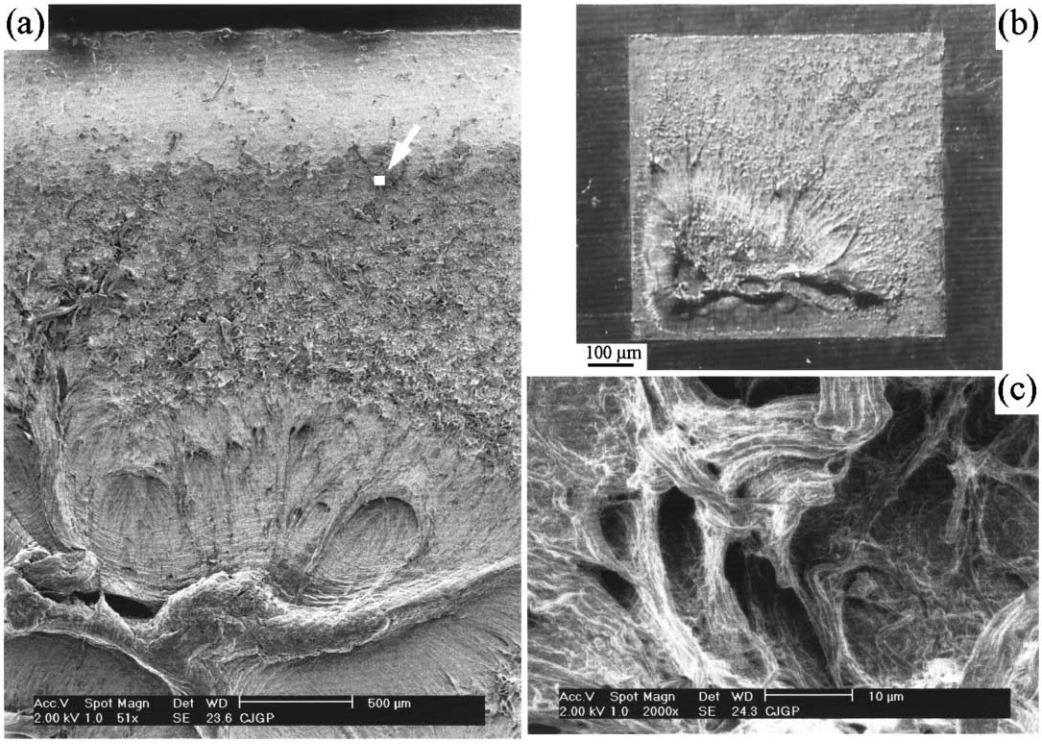

Fig. 9. Fracture surface of a PEB specimen tested at $\sigma_i = 3$ MPa and $K_i = 0.13$ MPam$^{1/2}$ in Igepal: (a) SEM of the fracture surface; (b) reflected light micrograph of the fracture surface; (c) detail of the fracture surface (the region indicated in (a)).

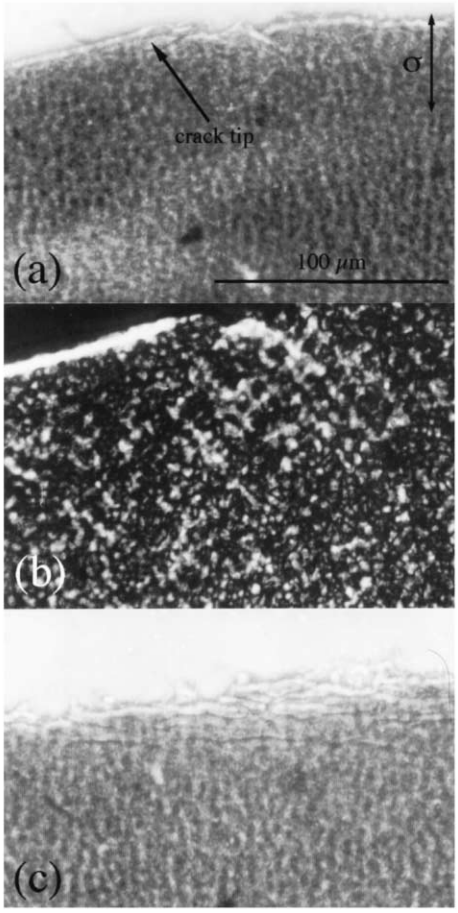

Fig. 10. OM of deformation in transverse sections through the fracture surface of a PEB specimen tested at $\sigma_i = 3$ MPa and $K_i = 0.12$ MPam$^{1/2}$ in Igepal: (a) phase contrast image from the notch tip; (b) the same region observed between crossed polarisers; (c) phase contrast image from in front of the notch tip (tensile axis as indicated by the arrows).

increased density of fine fibrils in the interior of the coarse voids in Fig. 8(c) compared with those in Fig. 6(d), but this was difficult to quantify.

3.3. FNCT fracture surfaces in Igepal (series PE3, PE4 and PE5)

Figs. 9–11 show the fracture surface of a PEB specimen tested in Igepal at $\sigma_i = 3$ MPa and $K_i = 0.12$ MPam$^{1/2}$, which failed after 2523 h. The fracture surface appeared relatively smooth at low magnifications and macroscopic necking was restricted. (The neck was displaced to one side of the fracture surface in this specimen owing to slightly asymmetric loading conditions during crack propagation.) Deformation below the fracture surface in the peripheral regions took the form of fine crack-like deformation zones at and immediately below the fracture surface, growing roughly parallel to this latter (Fig. 10). The images in Fig. 10(a) and (b) indicate little apparent blunting at the notch tip, the layer of oriented material visible on the left-hand side of Fig. 10(b) being due to the notching procedure.

The TEM micrographs shown in Fig. 11 were taken from sections through the fracture surface in Figs. 8 and 9 at about 2 mm from the notch tip, and were typical of the whole of the fracture surface with the exception of the central neck. The more heavily stained regions of the thin sections contained small, roughly equiaxed voids, and intervening undeformed or relatively undeformed lamellae are visible as light bands within these regions (Fig. 11(a)). The deformation zones were relatively diffuse, and their internal structure was closely correlated with that of the matrix. Where the dominant lamellae were locally at a high angle to the loading direction, they remained intact during the initial stages of deformation, so that we might loosely refer to this as 'interlamellar cavitation'. On the other hand, lamellae parallel to the loading direction were cleaved where they intersected the deformation zones. A detail from a region that had undergone interlamellar cavitation is shown in Fig. 11(b). Fibrillar texture is visible between the dominant lamellae in this micrograph, this presumably having resulted from drawing of the interlamellar material (including any secondary lamellae present). The lamellae perpendicular to the stress axis also showed some fragmentation within the deformed regions. This was thought to be at least partly due to the development of localised shear stresses within the lamellae in the presence of the voids, leading to what is sometimes referred to as 'block slip' [18,19]. However, as will be seen later, close examination of the base of micro-necks in the relatively coarse fibrillar deformation zones observed at higher K indicated block slip not to be contingent on interlamellar voiding.

Fig. 11(c) is less typical of the deformation in this specimen, but of interest in that the cavitation was relatively coarse (region (i), for example) owing to the local agglomeration of carbon black particles visible in the micrograph. The fine interlamellar fibrillation seen in Fig. 11(b) is present elsewhere in this micrograph (region (ii)). At the fracture surface, shown in Fig. 11(d), extensive fragmentation of lamellae by block slip or cleavage was visible, the lamellae being almost entirely reduced to small, roughly equiaxed fragments. This is often assumed to be a precursor to craze formation in semicrystalline polymers [20]. However, in Fig. 11(d) fracture intervened locally before the network of lamellar fragments and interlamellar fibrils was able to develop into the drawn fibrillar structure implicit in most definitions of crazing.

Fig. 12 shows deformation in a PEB specimen taken from an extruded pipe and tested under the same conditions as the specimen in Figs. 9–11. In this case, the specimen failed after 1175 h, indicating a somewhat reduced resistance to SCG compared with that of the compression moulded sheets. Fig. 12(a) shows a detail from a deformation zone in which both lamellar block slip (region (i) for example) and lamellar cleavage (region (ii)) were particularly apparent. Fig. 12(b) shows a section through the fracture surface itself from about 1 mm ahead of the notch, showing somewhat more extensive deformation than in Fig. 11(d).

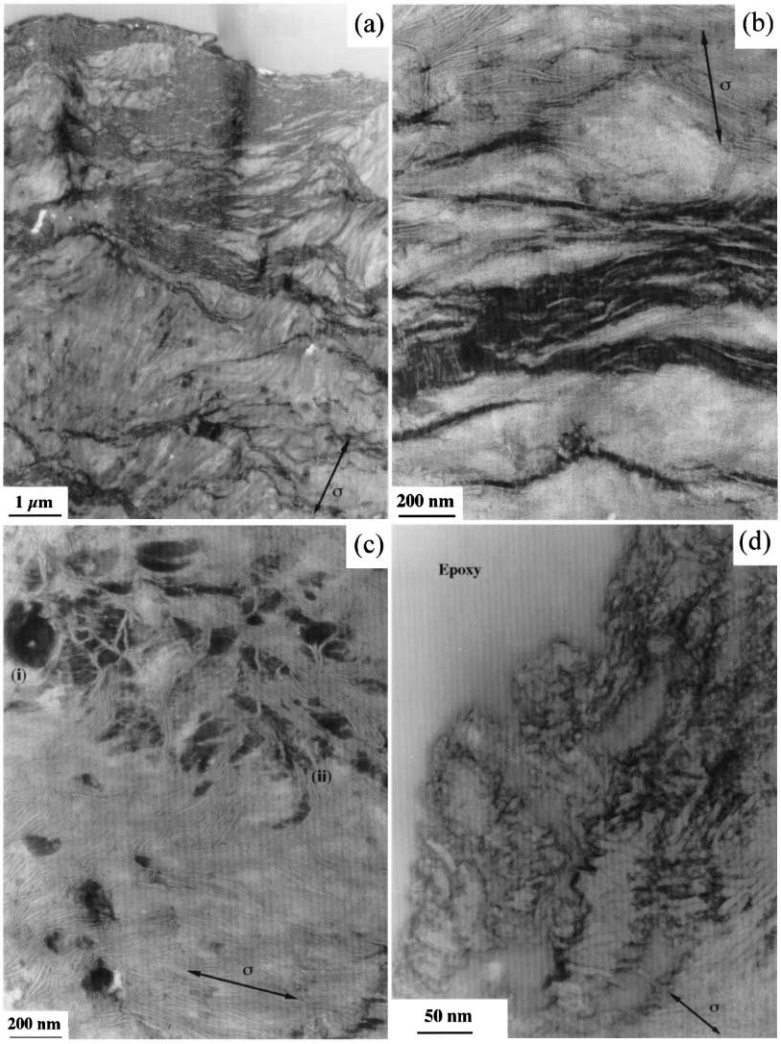

Fig. 11. TEM of a section through part of the fracture surface of a PEB specimen tested at $\sigma_i = 3$ MPa and $K_i = 0.12$ MPam$^{1/2}$ in Igepal: (a) overview; (b) localised interlamellar cavitation behind the fracture surface; (c) region of relatively diffuse deformation behind the fracture surface, showing both relatively coarse cavitation (i) and finer interlamellar cavitation (ii); (d) detail of deformation at the fracture surface (tensile axis as indicated by the arrows).

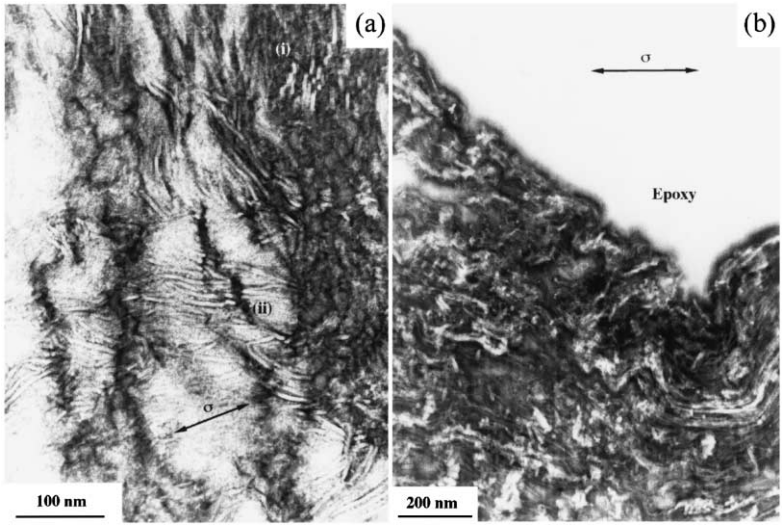

Fig. 12. TEM of a section through part of the fracture surface of an extruded PEB specimen tested at $\sigma_i = 3$ MPa and $K_i = 0.12$ MPam$^{1/2}$ in Igepal: (a) detail of deformation in behind the fracture surface; (b) detail of deformation at the fracture surface (tensile axis as indicated by the arrows).

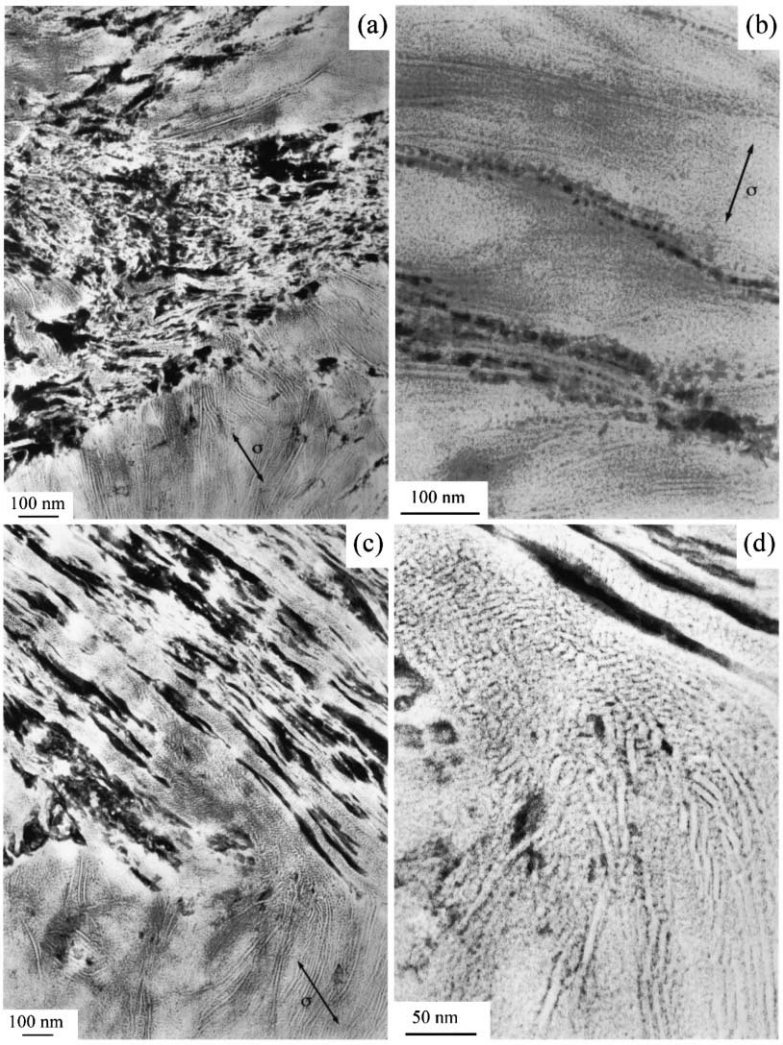

Fig. 13. TEM of a sections through the fracture surface of a PEB specimen tested at $\sigma_i = 5.4$ MPa and $K_i = 0.23$ MPam$^{1/2}$ in Igepal: (a) deformation behind the fracture surface close to the notch; (b) detail from close to the notch showing interlamellar cavitation; (c) coarse fibrillation close to the centre of the fracture surface; (d) detail of deformation at the base of one of the fibrils shown in (c) (tensile axis as indicated by the arrows).

A relatively mature fibrillar structure (albeit buckled) is visible in the bottom right hand corner of this figure, thought to reflect the craze formation mechanism referred to above.

Fig. 13 shows deformation in a compression moulded PEB specimen tested in Igepal at $\sigma_i = 5.4$ MPa and $K_i = 0.22$ MPam$^{1/2}$, which failed after 210 h. In this case, the fibrillar deformation was globally much coarser than in the same grade tested in Igepal at $K_i = 0.12$ MPam$^{1/2}$. Fibrillation on the scale of the lamellar texture and occasional stable zones of interlamellar cavitation were visible close to the notch tip, as shown in Fig. 13(a) and (b). However, towards the centre of the fracture surface for $K_i = 0.22$ MPam$^{1/2}$ the texture was more reminiscent of that seen in PEA and PEB tested in air. This is shown in Fig. 13(c); although the fibrillar structure had collapsed after unloading in this case, fibrillation was clearly on a scale much greater than that of the initial lamellar texture. The early stages of lamellar deformation were particularly evident at the base of the larger fibrils in this specimen. Fig. 13(d), for example, shows the block slip of the dominant lamellae in the absence of local interlamellar cavitation referred to in the context of Fig. 11.

The behaviour of PEA tested in Igepal at $\sigma_i = 3.1$ MPa and $K_i = 0.13$ MPam$^{1/2}$ was again similar to that of PEA and PEB tested in air. There was substantial necking prior to ultimate failure, which occurred after 10 h, and, as shown in Fig. 14, severe cavitation behind the neck at the centre of the fracture surface. The peripheral region of fibrillar deformation was very similar to that in Fig. 5, for example, with progressively finer fibrillation towards the notch tip. TEM nevertheless confirmed the stable interlamellar cavitation characteristic of PEB deformed under these conditions to be absent. It should be mentioned for completeness that the specimen shown in Fig. 14 was not carbon black filled. However, with the exception of isolated regions of localised damage such as that shown in Fig. 11(c), the nature and

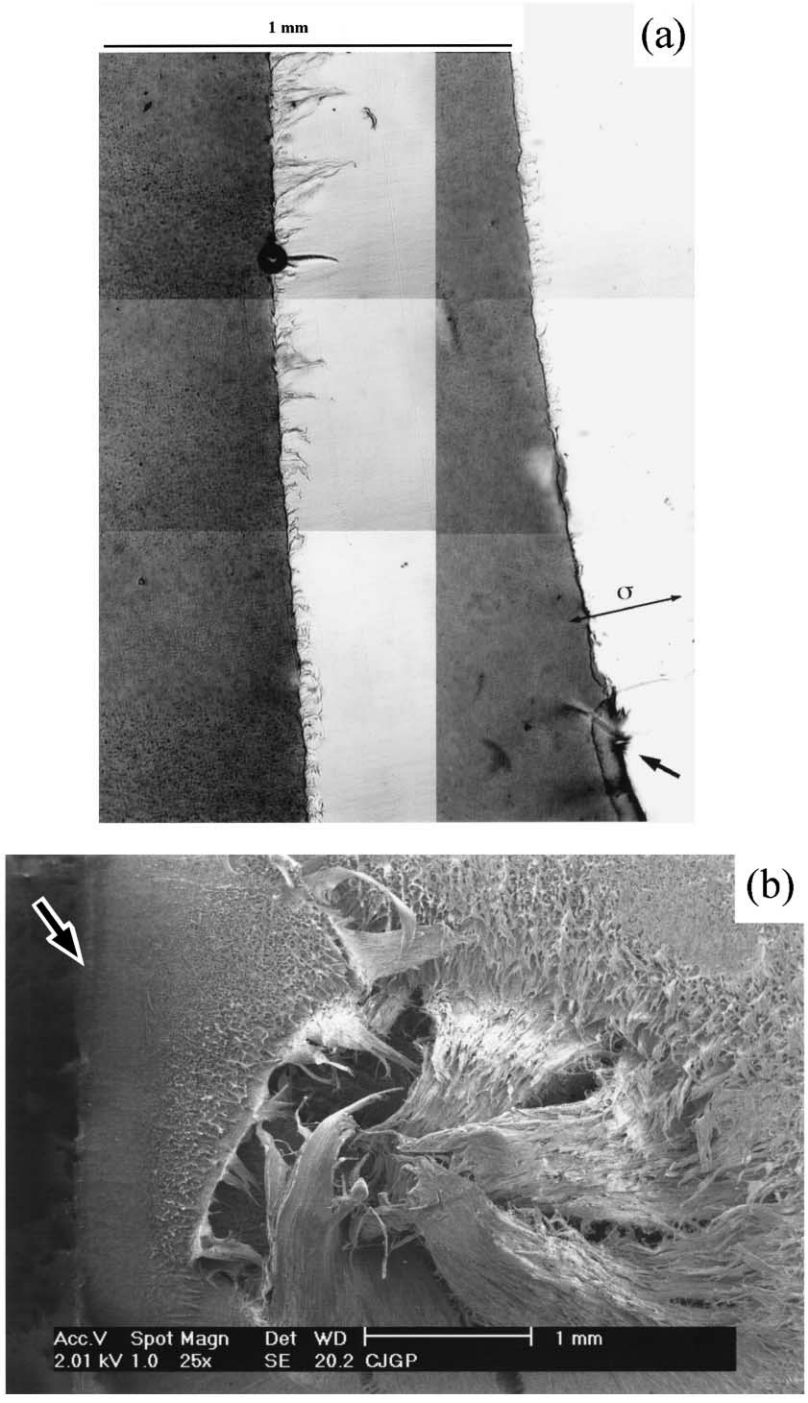

Fig. 14. Overview of the fracture surface of a PEA specimen tested at $\sigma_i = 3.1$ MPa and $K_i = 0.13$ MPam$^{1/2}$ in Igepal: (a) transmitted light OM of a section through the fibrillar region; to save space, two contiguous parts of the section are shown side by side; the top left-hand corner of the figure corresponds to the interior of the fracture surface and the bottom left-hand corner includes the notch tip, indicated by the arrow; (b) SEM of the fracture surface, with the notch tip indicated by the arrow.

extent of microdeformation were not observed to be correlated with the presence of the filler particles.

4. Discussion

The deformation induced structures at the crack tip described in the previous section varied considerably in scale, ranging from diffuse zones of interlamellar deformation with fibril dimensions roughly commensurate with the lamellar spacing (or thickness) of about 10 nm, to craze-like deformation zones with fibril diameters of 0.1 mm or more. Indeed the central macroscopic necks observed in all the specimens may be considered to represent the limiting

case of the trend towards coarser fibrillation at higher stresses. The applied stress is also known to influence the craze fibril spacing in glassy polymers, this having been interpreted in terms of a unique surface instability mechanism for fibril formation [21,22]. However, the extended range of fibril diameters and spacings observed during SCG in HDPE suggests that it may be more realistic to consider fibrillation in this case to involve two or more distinct damage mechanisms, as will be described in what follows. Moreover, the smallest fibril diameters were associated with relatively low K in the present tests, whereas the opposite is generally true of craze fibrils in glassy polymers [22].

The characteristics of the different regimes of SCG described in the previous section may be summarised in more detail as follows:

1. In the peripheral regions of the fracture surfaces of compression moulded PEB tested at $K_i = 0.12\ \mathrm{MPam}^{1/2}$ in Igepal, SCG occurred via breakdown of interlamellar fibrils, after widespread interlamellar voiding.
2. In the central regions of the fracture surface of PEB (where $K > K_i$) tested at $K_i = 0.12\ \mathrm{MPam}^{1/2}$ in Igepal and the outer regions of the fracture surface of the same grade tested at $K_i = 0.22\ \mathrm{MPam}^{1/2}$ in Igepal, widespread interlamellar voiding occurred, but the interlamellar fibrils initially remained relatively stable with respect to crack formation. Continued drawing of material containing fragmented lamellae and interlamellar voids led to craze-like structures prior to fracture. This type of deformation has also been observed in the periphery of the fracture surfaces of specimens of a medium density PE (MDPE) tested at $K_i = 0.12\ \mathrm{MPam}^{1/2}$ in Igepal, and whose resistance to SCG was intermediate between that of PEA and PEB [23].
3. Coarse fibrillation was seen at the centre of the fracture surfaces of PEB tested at $K_i = 0.22\ \mathrm{MPam}^{1/2}$ in Igepal, in the periphery of the fracture surfaces of PEA tested at $K_i = 0.12\ \mathrm{MPam}^{1/2}$ in Igepal and in the periphery of the fracture surfaces of PEA and PEB tested in air at $K_i = 0.2$ and $0.25\ \mathrm{MPam}^{1/2}$. It was assumed to result from fibrillation by breakdown of the interlamellar material without prior interlamellar voiding. This was inferred from both the lack of lamellar fragmentation and the lack of interlamellar voiding beyond the interface between the main damage zones and the surrounding material. The voids became coarser as K increased, leading to morphologies in which the deformed matrix ligaments formed continuous sheets rather than fibrils, and eventually to macroscopic necking.

The sequence of mechanisms, sketched in Fig. 15, or the preponderance of a given mechanism, will be governed by the K dependence of the various processes involved. Fig. 16 provides a qualitative representation of the competition

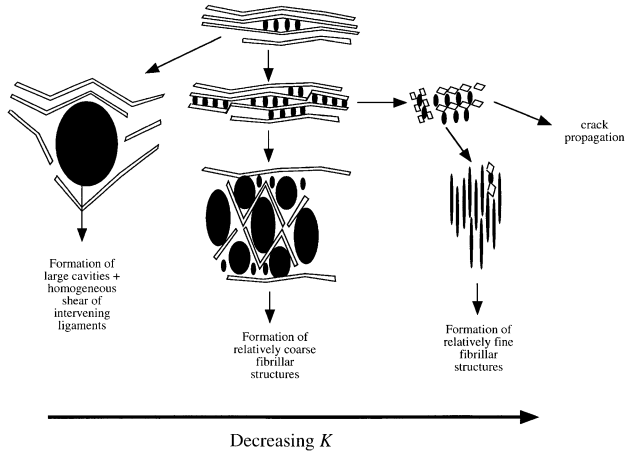

Fig. 15. Schematic of the proposed damage mechanisms as a function of K.

between these different mechanisms as a function of K_i, based on the above observations. The time to yield increases rapidly as the global stress falls below the short-term yield stress, which is represented by an equivalent K value, K_y. The appearance of interlamellar cavitation in the PEB grade at relatively low K after long times is assumed to reflect a relatively strong strain rate dependence of the local stress required for cavitation. The effective stress for interlamellar fibrillar breakdown is therefore taken to be greater than that for interlamellar cavitation at long times, although the curves for the respective mechanisms presumably cross over at some intermediate time, as suggested in Fig. 16.

The crossover of the curves for cavitation and interlamellar fibrillar breakdown corresponds to the onset of the regime of coarse fibrillation. In this regime, breakdown of the interlamellar regions prior to macroscopic necking is not thought to lead to immediate macroscopic failure for two reasons. First, the onset of the instability depends on the local lamellar orientation and second, the accompanying changes in the local stress state may promote plastic deformation rather than further rupture. A synergy between local drawing and decohesion (by chain scission or by disentanglement) is also implicit in some current models for crazing in amorphous polymers [22,24]. Hence if breakdown of interlamellar material in HDPE under the present conditions results from disentanglement, as has often been suggested in the past [7,25], there is a strong analogy between this mode of deformation and disentanglement crazing in glassy polymers [24,26,27]. Both modes of deformation are favoured over bulk necking by high temperatures and long times (or low strain rates). Indeed, at temperatures just below T_g, modes of diffuse local cavitation have also been identified in certain glassy polymers, these sometimes being referred to as 'intrinsic crazing' [28]. At higher stresses, however, where HDPE becomes very unstable with respect to the formation of large voids, a better analogy might be with a rubber toughened system in which the second phase undergoes extensive cavitation. In the case of an unmodified semicrystalline polymer, microstructural features such as

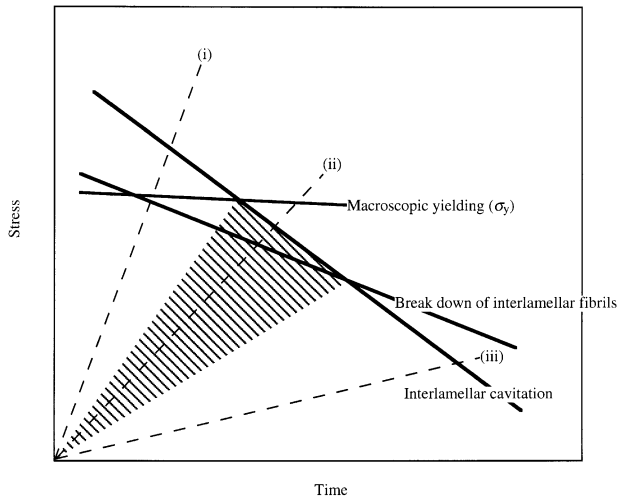

Fig. 16. Schematic of the proposed relative load-time dependence of the basic damage mechanisms of SCG in HDPE. A sample loaded relatively rapidly (loading line (i)) will reach its macroscopic yield stress first and undergo macroscopic necking, with ultimate failure occurring by ductile tearing. Loading line (ii) first intercepts the load-time curve for breakdown of interlamellar fibrils, but this process can only initiate after formation of interlamellar voids at a somewhat higher load, leading to an instability and coarse fibrillation as described in the text, as will any load line within the hatched region. Loading line (iii), on the other hand, intercepts the load-time curve for interlamellar cavitation first and stable zones of interlamellar cavitation are therefore expected to be present behind the fracture surface. Also, if the load at which breakdown of interlamellar fibrils occurs is well below the yield stress, there will be little further drawing down of these zones prior to ultimate failure.

the spherulite diameter or local fluctuations in the lamellar orientation presumably determine the void distribution. In SCG in polyoxymethylene (POM), for example, in which similar mechanisms have been evoked to account for the formation of fibrillar damage zones, fibril diameters at intermediate K are thought to be linked to local correlations in the lamellar trajectories on a scale of about 10 lamellar thicknesses, giving a stacked lamellar morphology [25].

Stable interlamellar cavitation was not seen in specimens of the PEA grade under any of the conditions investigated here. To explain this, it is reasonable to invoke the absence of the long, branched chains thought to be characteristic of the high molar mass fraction of the PEB grade. This is expected to reduce the resistance of the interlamellar material to breakdown by disentanglement, so that the corresponding curves should be displaced as shown in Fig. 16. (It is unclear whether zones of stable interlamellar fibrillation are totally suppressed in PEA, since data are still lacking for the behaviour in the low K_i limit for this material in Igepal.) There is less reason to suppose a priori the molecular weight distribution to have a dominant influence on interlamellar cavitation, which occurs at more local length scales and is hence expected to be primarily dependent on factors such as the effective cohesive energy density, for example [29]. The resistance to SCG itself is not necessarily directly linked to interlamellar cavitation, but the ultimate breakdown of all types of fibrillar or necked structure will also reflect the instability of the interlamellar material.

The above discussion is based on the assumption that the specimens tested in Igepal did indeed reflect the limiting behaviour at low K in air. Up to now we have not been able to provoke the formation of stable regions of interlamellar cavitation in PEB in air under creep conditions. However, in studies of microdeformation during accelerated testing by fatigue loading [30], very similar structures to those in Fig. 11 have been observed close to the notch tips of PEB tested at low K_i. They are therefore not uniquely a consequence of Igepal. G'Sell et al. have also reported similar changes to be associated with a transition to continuous SCG in fatigue experiments on PEA with $K_{max} \approx 0.2\ MPam^{1/2}$, the continuous regime again being characterised by relatively smooth fracture surface [31]. The transition from interlamellar cavitation to coarse cavitation observed in the PE4 specimen tested in Igepal at high K_i, also shows that both mechanisms may occur in the same specimen under suitable conditions. Igepal therefore does not necessarily lead to stable interlamellar fibrillation in PEB, depending on the effective value of K.

5. Conclusions

In notched HDPE specimens subject to static loading, high stress, short-term failure is initiated by yielding across the whole of the load-bearing ligament, accompanied by coarse cavitation in the specimen interior. As K decreased, there was a transition to SCG, characterised by the formation of a fibrillar crack tip damage zone. The fibrils became progressively finer as K decreased further, and in notched specimens of a relatively tough, 3rd generation pipe grade tested for about a month at 80°C in Igepal at low K_i, the fracture surfaces appeared smooth, crack propagation being associated with localised interlamellar cavitation. The existence of zones of stable interlamellar cavitation behind the main crack front was assumed to reflect the relative stability of the interlamellar fibrils in this grade under these conditions. (It may prove to be more appropriate to refer to cavitation or fibrillation between dominant lamellae here, but this point has not yet been explored fully.) Direct interlamellar breakdown without prior cavitation has been argued to be at the origin of coarser cavitational mechanisms observed in a less resistant 1st generation pipe grade under the same conditions, and in both the 1st and the 3rd generation pipe grades tested in air at higher loads. The difference in behaviour of the two grades was attributed to the relative ease of disentanglement in the 1st generation pipe grade.

The present work is nevertheless based on a relatively limited number of specimens tested under a limited range of conditions, and certain of the above hypotheses require confirmation by more extensive testing. In particular it would be interesting to look at the long-term behaviour in

Igepal of the 1st generation pipe grade at relatively low K_i, in order to investigate the eventual presence of stable inter-lamellar cavitation. It would also be interesting to examine in more detail any eventual microstructural differences between the different grades in the light of their different microdeformation behaviour (segregation of different molar mass fractions and the dominant-secondary lamellar structure). Moreover, the question of the fundamental reasons for accelerated crack growth in the presence of Igepal has not been addressed. This would clearly be necessary in any attempt to establish a firm link between accelerated and un-accelerated crack growth behaviour. Nevertheless, identification of the relevant damage mechanisms and their dependence on K represents an important step in this direction.

Acknowledgements

We acknowledge the financial support of Solvay Polyolefins Europe, Belgium throughout this work and the technical support of the Interdepartmental Centre of Electron Microscopy of the EPFL.

References

[1] Scheirs J, Böhm LL, Boot JC, Leevers PS. Trends Polym Sci 1996;4:408.
[2] Ward AL, Lu X, Huang Y, Brown N. Polymer 1991;32:2172.
[3] Fleissner M. Polym Engng Sci 1998;38:330.
[4] Arnold JC. Trends Polym Sci 1996;4:403.
[5] Brown WF, Crawley JE. AST STP 1966;410:15.
[6] Cawood MJ, Channell AD, Capaccio G. Polymer 1993;34:423.
[7] Brown N, Lu X. Polymer 1995;36:543.
[8] Nishio N, Imura S, Yashura M, Nagatani F. Proc 9th Plastic Fuel Gas Pipe Symp 1985:29.
[9] Duan D-M, Williams JG. J Mater Sci 1998;33:625.
[10] Iimura S, Akiyama S, Kasahara K. Proc 11th Plastic Fuel Gas Pipe Symp 1989:421.
[11] Nishimura H, Narisawa I. Polym Engng Sci 1991;31:399.
[12] Goldberg A, Hellinckx S. Internal Report, Solvay Polyolefins Europe and Solvay, 2000.
[13] Beech SH, Palmer SJ, Burbidge RW. Int Plastic Pipe Symp 1997:205.
[14] Drèze H, Scheelen A. Int Plastic Pipe Symp 1998:10.
[15] Chan MKV, Williams JG. Polymer 1983;24:234.
[16] Bassett DC. Principles of polymer morphology. Cambridge: Cambridge University Press, 1981.
[17] Brown HR. Macromolecules 1991;24:2752.
[18] Brady JM, Thomas EJ. J Mater Sci 1989;24:3311.
[19] Brady JM, Thomas EJ. J Mater Sci 1989;24:3319.
[20] Friedrich K. In: Kausch H-H, editor. Advances in polymer science, vol. 52/53. Berlin: Springer, 1983. Chapter 5.
[21] Kramer EJ. Polym Engng Sci 1984;24:761.
[22] Kramer EJ. In: Kausch H-H, editor. Advances in polymer science, vol. 52/53. Berlin: Springer, 1983. Chapter 1.
[23] Plummer CJG. Internal Report, Solvay Polyolefins Europe and Solvay, 1999.
[24] Kramer EJ, Berger LL. In: Kausch H-H, editor. Advances in polymer science, vol. 90/91. Berlin: Springer, 1990. Chapter 1.
[25] Plummer CJG, Scaramuzzino P, Kausch H-H. Polym Engng Sci 2000;40:1306.
[26] Plummer CJG, Donald AM. Macromolecules 1990;23:3929.
[27] Donald AM. J Mater Sci 1985;20:2634.
[28] Dettenmaier M. In: Kausch H-H, editor. Advances in polymer science, vol. 52/53. Berlin: Springer, 1983. Chapter 2.
[29] Van Krevelen DW. Properties of polymers. Amsterdam: Elsevier, 1976.
[30] Plummer CJG, Ghanem A, Goldberg A. In prepration.
[31] G'Sell C, Favier V, Giroud T, Hiver JM, Goldberg A, Hellinckx S. In: Proceedings of the 11th International Conference on Deformation, Yield and Fracture of Polymers, Cambridge, UK, 10–18th April, 2000. p. 73.